RUTHERFORD BACKSCATTERING IN ION-IMPLANTED AND PULSED LASER ANNEALED Si AND Ge

by

SHANALYN KIGER

B.S., Kansas State University, 1984

A MASTER'S THESIS

submitted in partial fulfillment of the

requirements for the degree

MASTER OF SCIENCE

Department of Physics

KANSAS STATE UNIVERSITY

Manhattan, Kansas

1985

Approved by:

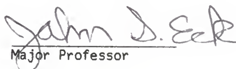

Major Professor

LD
2668
.T4
1985
K53
c. 2

TABLE OF CONTENTS

A11202 641502

Page

LIST OF FIGURES ii

LIST OF TABLES iii

ACKNOWLEDGEMENTS iv

Chapter

I. INTRODUCTION 1

A. SEMICONDUCTOR DOPING 2

B. ANNEALING 3

II. RUTHERFORD BACKSCATTERING 5

A. KINEMATIC FACTOR 5

B. ENERGY LOSS 11

C. SENSITIVITY 15

III. EXPERIMENT 17

A. $^{4}He^{+}$ RBS 17

B. $^{19}F^{4+}$ HIRBS 25

IV. DATA ANALYSIS 29

A. X-AXIS SCALES 37

B. Y-AXIS SCALES 40

V. RESULTS 55

VI. CONCLUSION 72

ABSTRACT

LIST OF FIGURES

		Page
Fig 1.	RBS spectrum of Si:As, 1×10^{17} As cm^{-2}	6
2.	Graph of the kinematic factor vs. backscattering angle	9
3.	RBS spectrum of Ge:In, 1×10^{16} In cm^{-2}	9
4.	Graph of the kinematic factor vs. incident mass	12
5.	Graph of energy loss vs. incident mass	16
6.	Graph of differential cross section vs. incident mass	20
7.	Schematic of 3MV Van de Graaff accelerator	23
8.	Schematic of Tandem Van de Graaff accelerator	26
9.	RBS spectrum of Si:As, 1×10^{17} As cm^{-2}	30
10.	HIRBS spectrum of Ge:Bi, 1×10^{16} Bi cm^{-2}	30
11.	Schematic of spectrum with pile-up	32
12.	HIRBS spectrum of Ge:Bi, 1×10^{16} Bi cm^{-2}	35
13.	HIRBS spectrum of Ge:Bi, 1×10^{16} Bi cm^{-2} stripped of pile-up and condensed	35
14.	HIRBS spectrum of annealed Ge:Bi, 1×10^{16} Bi cm^{-2}	38
15.	HIRBS spectrum of as-implanted Ge:Sb, 2×10^{16} Sb cm^{-2}	43
16.	a-d) HIRBS spectra of Ge:In	45
17.	a-f) HIRBS spectra of Ge:Sb	47
18.	a,b) HIRBS spectra of Ge:Bi	49
19.	a-d) RBS spectra of Si:As	51
20.	a-d) RBS spectra of Si:In	53
21.	a-e) HIRBS relative density spectra of Ge samples	60
22.	Schematic of equilibrium phase diagram for the implant plus substrate systems	66

LIST OF TABLES

page

table 1 Surface backscattered energies and depth conversions of the target elements 41

2 Projected ranges and standard deviations of impurity elements in Si 56

3 Comparison of as-implanted and annealed impurity elements 57

4 Projected ranges and standard deviations of impurity elements in Ge 58

5 Comparison of as-implanted and annealed impurity peak FWHM values in Ge 65

6 Maximum impurity concentrations obtained by pulsed laser annealing compared to retrograde solubility limit 70

7 Comparison of predicted and measured impurity dose in Ge samples 71

ACKNOWLEDGEMENTS

This thesis would not have been possible without the support of the faculty and staff at Kansas state University.

I wish to thank my advisor, Dr. John Eck, and my committee members, Dr. Alvin Compaan and Dr. Brock Dale, for their guidance and encouragement. Thanks also go to Dr. Basil Curnutte for his help on the many repairs required by Baby Huey. Finally, I would like to thank Joyce Martin for her expert typing at such a busy time for all of us.

Chapter 1

INTRODUCTION

A knowledge of the impurity atoms distribution as a function of depth in a semiconductor substrate is extremely important in the design and fabrication of semiconductor devices. A depth profile can be obtained using Rutherford backscattering techniques in which an ion beam of known energy, charge, and atomic mass number is incident upon a sample. The energy of the ions which undergo elastic collisions within the sample is measured at an angle greater than 90° with respect to the incident beam. This produces a spectrum of peaks corresponding to the sample elements as a function of energy which can be converted to mass or depth.

Traditionally such measurements are done using small accelerators ($<3MV$) with proton or alpha particle beams. However if, instead of Si, a heavier substrate such as Ge is to be measured, the Rutherford backscattering resolution with proton or alpha beams is often not sufficient to distinguish the impurity peak from the substrate peak. From the equations used in Rutherford backscattering analysis, it is apparent that an increase in the ion beam mass will result in better mass resolution, better depth resolution, and an increased sensitivity to the impurity atoms within the Ge substrate.

In this thesis, the depth profiles of as-implanted and pulsed laser annealed Si and Ge samples, doped with various impurities, are studied using Rutherford backscattering and heavy ion Rutherford backscattering.

SEMICONDUCTOR DOPING

One of the first steps in semiconductor fabrication is the introduction of impurity atoms into a semiconductor substrate. Traditionally this is done by a diffusion method in which the substrate is placed in an environment of high dopant concentration and elevated temperature whereby the impurity atoms diffuse into the crystal. Because this is an equilibrium process, not all types of impurity atoms will diffuse into the substrate, and the concentration of those that will diffuse is limited by the solid solubility value. The distribution obtained from diffusion will be monotonically decreasing as a function of distance from the surface with the maximum concentration at the surface. Clearly, important parameters such as the dosage and distribution of impurity atoms are not easily manipulated in this process.

An alternative to diffusion is ion implantation. In this method a beam of ions is accelerated to a desired energy and then directed onto a semiconductor surface at a specified angle. The beam current is monitored so that a precise dopant dose can be obtained. The ions, upon collision with the substrate, will deccelerate due to atomic and nuclear scattering and will eventually come to rest in the lattice. The distribution is approximately Gaussian, and characteristics such as the projected range and projected standard deviation of the impurity ions in the substrate can be obtained from nuclear data tables given the beam energy, beam mass, and target mass. This method does not limit the type of ions to be introduced and a higher impurity concentration than from diffusion techniques is possible. By varying the ion type and energy, the distri-

bution can be shaped to approximate the ideal step function. Thus it is easy to see the advantages of implantation over diffusion.

However, ion implantation also has a major disadvantage. As the ion beam traverses the substrate, it loses energy through atomic and nuclear scattering. Generally atomic scattering is the dominant energy loss mechanism for high energy ions and nuclear scattering for low energy ions. In atomic scattering, a beam ion may excite or eject electrons from target atoms in the substrate but will produce little damage to the crystal structure. On the other hand, in a nuclear collision a beam ion can transfer enough energy to a substrate atom to displace it from its lattice site. Consequently a beam ion produces a path of lattice damage as it traverses the substrate. The periodic lattice structure must be restored and the impurity ions made substitutional (as opposed to interstitial) so that they can be electrically activated.

ANNEALING

There are a number of ways to repair the damaged semiconductor crystal: thermal annealing, continuous wave laser annealing, and pulsed laser annealing. Thermal annealing is traditionally used in semiconductor device processing because it can be easily incorporated into mass production systems. Once again thermal annealing is an equilibrium process and as such the maximum concentration of substitutional impurities will have as an upper bound the solubility limit. All non-substitutional dopants will segregate to the surface or precipitate in clusters. Moreover, because thermal annealing requires that the temperature of the entire crystal be elevated, this might disturb other previously doped areas and contacts on the substrate.

Continuous wave laser annealing resolves this last problem because it is more localized. However it too is an equilibrium process and will have a corresponding maximum obtainable concentration.

On the other hand, pulsed laser annealing is not an equilibrium process. Experiments have shown that with pulse duration on the order of 10 nsec, the liquid-solid interface moves to the surface at a rate of several meters per second. At this rate the impurity ions are effectively "trapped" in lattice sites, resulting in a maximum concentration higher than that obtained from other methods of annealing. The energy density and duration of the pulse determines the melt depth which must exceed the damage depth to assure epitaxial regrowth.[1] The number of laser pulses delivered to one spot on the crystal can affect the dopant distribution by allowing the impurity atoms more time to diffuse in the melt. These parameters can be varied to obtain a desired impurity concentration and distribution as a function of depth into the crystal.

Chapter 2

RUTHERFORD BACKSCATTERING

Rutherford backscattering (RBS) provides a method of observing the impurity atom concentration and distribution as a function of depth in the crystal. A beam of ions of a particular mass and energy is directed onto the target. The beam can backscatter off target atoms whose mass is greater than the beam mass. Finally the energy of the backscattered beam is measured. An example of the spectrum obtained is shown in Fig. 1. The x axis has units of channels, which is proportional to the backscattered energy.

Fig. 1 was obtained with a He beam at an incident energy of 1.5 MeV. This is a commonly employed method because small accelerators (less than 3MV) using He or H beams are readily accessible. The spectrum in Fig. 1 exhibits good kinematic separation of the target element peaks; that is, the Si substrate peak is easily distinguished from the implant peak. Good kinematic separation is necessary to observe the impurity distribution both before and after annealing.

KINEMATIC FACTOR

The kinematic factor, K, is the ratio of the ion beam's backscattered energy, E , to its incident energy, E . The expression for K in the laboratory frame is

$$K = \frac{E_1}{E_o} = \left\{ \frac{(m_2^2 - m_1^2 \sin^2\psi)^{\frac{1}{2}} + m_1 \cos\psi}{m_1 + m_2} \right\}^2$$

Fig. 1 RBS spectrum of Si:As at a dose of 1×10^{17} As cm^{-2} using a 1.5 MeV ^4He beam, $\psi = 150^{\circ}$.

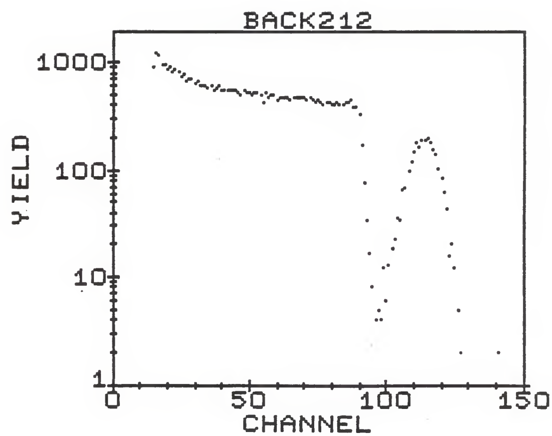
BACK212
1000
100
10
1
YIELD
0
50
100
150
CHANNEL

where m_1 is the incident ion mass

m_2 is the target mass

ψ is the scattered angle.

One method of improving the kinematic separation between the peaks of the target elements is to let the backscattering angle approach 180 degrees. This is most easily demonstrated in the graph of K vs ψ in Fig. 2 where each curve corresponds to a different target element. Clearly, as ψ approaches 180 degrees the absolute value of the difference between the kinematic factors increases. Thus from Fig. 1, it is apparent that the He^+ beam of 1.5 MeV at ψ=150 degrees is a sufficient method of determining an impurity distribution in a Si substrate.

However, it is obvious from Fig. 3 that the same method is not sufficient to distinguish an impurity peak from a Ge substrate peak, and certainly could not be used to determine the distribution of an impurity in a Ge crystal. The spectrum must be improved in two ways. First, the impurity peak should be well separated from the Ge substrate peak. Second, the height of the impurity peak relative to the Ge peak should be increased. This point will be examined later. The first point is a call for better kinematic separation and can be expressed quantitatively by the mass resolution.

For large backscattering angles, K can be approximated by [2]

$$K \simeq \left[\frac{m_2-m_1}{m_2+m_1}\right]^2 \left[1 + \frac{m_1}{m_2}\ \delta^2\right] = \left[\frac{1-x}{1+x}\right]^2 \left[1 + x\ \delta^2\right]$$

where $\delta = \pi - \psi$

$$x = \frac{m_1}{m_2}$$

Fig. 2 Graph of the kinematic factor vs. backscattering angle where each curve represents a different target element. The beam is a 17.5 MeV ^{19}F, $\psi = 150^{o}$.

Fig. 3 RBS spectrum of Ge:In at a dose of 1×10^{16} in cm^{-2} using a 1.5 MeV ^{4}He beam, $\psi = 150^{o}$.

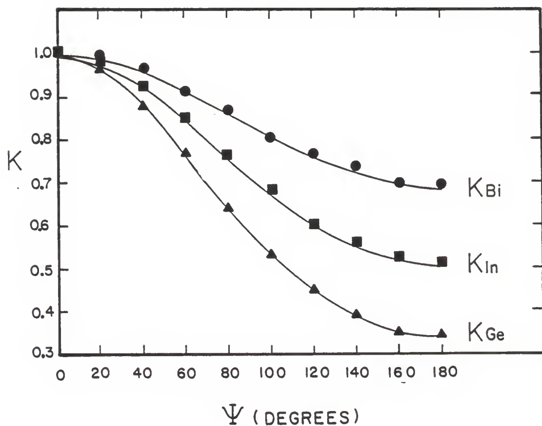
K
1.0
0.9
0.8
0.7
0.6
0.5
0.4
0.3
0
20
40
60
80
100
120
140
160
180
KBi
KIn
KGe
Ψ (DEGREES)

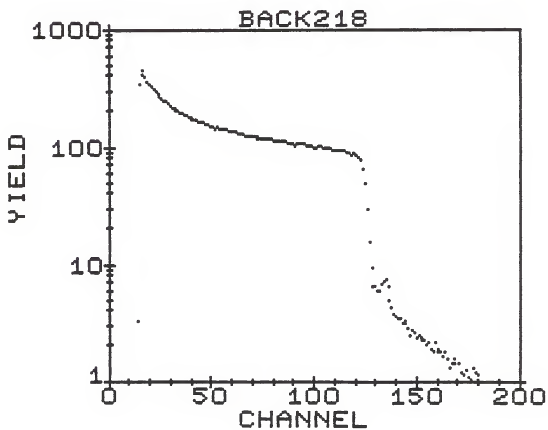
BACK218
YIELD
1000
100
10
1
0
50
100
150
200
CHANNEL

An expression for the mass resolution can be obtained if ΔE_1 is the change in energy between two target masses whose mass difference is Δm_2 Clearly it is desirable to have ΔE_1 to be large for a given Δm_2.

$$\Delta E_1 = E_0 \frac{dK}{dm_2} \Delta m_2$$

$$= E \frac{1-x}{(1+x)^3} \left[4(1 + x\delta^2) - \delta^2(1 - x^2) \right] \frac{x}{m_2} \Delta m_2$$

Now if x is small, ie. the target mass m_2 is much larger than the incident ion mass m_1, then

$$\Delta E_1 \simeq E_0 \ (4-\delta^2) \ \frac{m_1}{m_2^2} \Delta m_2$$

Thus for good mass resolution, $\Delta E_1/\Delta m_2$ must be large. This can be accomplished if E_0 and m_1 are large since $\Delta E_1/\Delta m_2$ is linear in E_0 and m_1. However it will be shown that the sensitivity of RBS decreases as E_0^2. Therefore a higher incident mass directly improves the RBS properties of kinematic separation, see Fig. 4, and mass resolution.

ENERGY LOSS

Up to this point only the backscattered energy from the surface of the target has been considered. This energy can be predicted if the masses, angle, and incident energy are known. However, below the surface the ions will lose kinetic energy both before and after scattering.

Fig. 4 Graph of the kinematic factor vs. incident mass where each curve represents a different target element. The 17.5 MeV ^{19}F beam backscatters at $\psi = 150^{\circ}$.

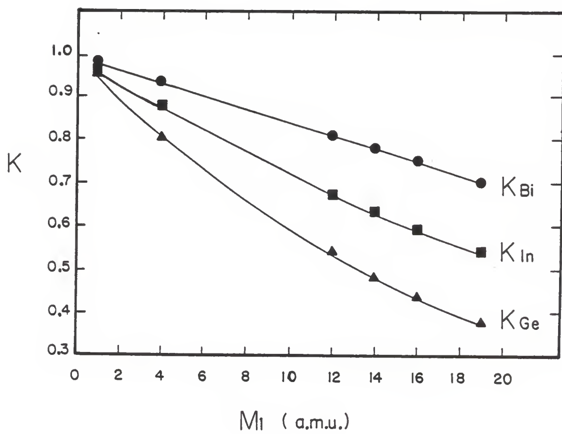
K
1.0
0.9
0.8
0.7
0.6
0.5
0.4
0.3
0
2
4
6
8
10
12
14
16
18
20
K Bi
K In
K Ge
M1 (a.m.u.)

The energy, $E(x)$, of a particle moving beneath the surface a distance x whose incident energy was E_0 is given as

$$E(x) = E_o - \int_o^x \frac{dE}{dx}\, dx$$

where dE/dx is the energy loss (or stopping power).

As an approximation for $E(x)$, the energy loss, dE/dx, can be considered constant over the distance x so that

$$E(x) = E_o - \left.\frac{dE}{dx}\right|_{E_o} x$$

This expression is only valid near the surface (ie. for small x) and is known as the surface approximation.

Using this last expression, it is possible to find an expression relating the change in energy to the change in depth.

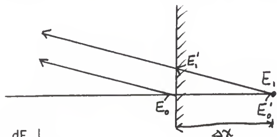

$$E_o' = E_o - \left.\frac{dE}{dx}\right|_{E_o} \Delta x$$

$$E_1 = KE_o'$$

$$E_1' = E_1 - \left.\frac{dE}{dx}\right|_{E_1} \frac{-\Delta x}{\cos\psi}$$

Combining these three equations, an expression for the depth resolution is obtained

$$\Delta E = \left[K \left.\frac{dE}{dx}\right|_{E_0} - \frac{1}{\cos\psi} \left.\frac{dE}{dx}\right|_{E_1}\right] \Delta x$$

$$\simeq \left[K - \frac{1}{\cos\psi}\right] \left.\frac{dE}{dx}\right|_{E_0} \Delta x$$

using the approximation $\left.\frac{dE}{dx}\right|_{E_1} \simeq \left.\frac{dE}{dx}\right|_{E_0}$

It is desirable to have dE/dx be large. From the graph in Fig. 5 it is clear that dE/dx increases with increasing m_1. Thus for a fixed angle, the depth resolution of RBS is improved by increasing the beam mass.

SENSITIVITY

Another characteristic of RBS that is enhanced when the beam mass, m_1, is increased is the sensitivity of the probing beam to the target atoms. this is a consequence of two effects.

First, returning to the equation for depth resolution,

$$\Delta x = \frac{\Delta E}{(K - \frac{1}{\cos\psi}) \left.\frac{dE}{dx}\right|_{E_0}}$$

Fig. 5 Graph of energy loss vs. incident mass for a 17.5 MeV beam on a ^{73}Ge target.[3]

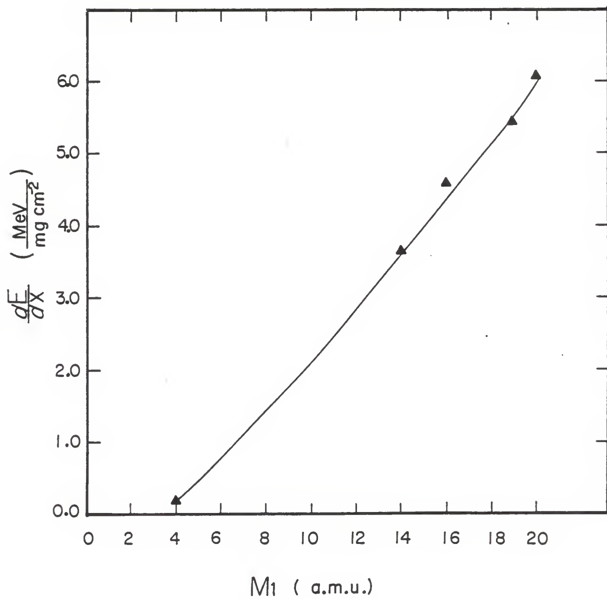
6.0
5.0
4.0
3.0
2.0
1.0
0.0
$\frac{dE}{dX}$ $\left(\frac{MeV}{mg\ cm^{-2}}\right)$
0
2
4
6
8
10
12
14
16
18
20
M1 (a.m.u.)

it is evident that, for a given incident energy, a heavier beam will travel a smaller distance than a lighter beam since dE/dx increases as the incident mass increases. Given that the impurity atoms are near the surface, the heavier beam will encounter more impurity atoms per substrate atom than the lighter beam. Thus the fact that the heavy incident ions traverse a smaller distance than the light ions makes them a more sensitive probe to the impurity atoms.

Second, the elemental yield can be expressed as follows

$$Y = Y_0 \frac{d\sigma}{d\Omega} \, d\Omega \, Nt$$

where $d\sigma/d\Omega$ is the differential cross section

Y_0 is the number of incident particles

N is the density

t is the thickness of the measured interval

In a sample consisting of a substrate and an implanted impurity, the ratio of the detected impurity atoms to those of the substrate is proportional to the ratio of the cross sections

$$\frac{Y_{imp}}{Y_{sub}} \propto \frac{d\sigma_{imp/d\Omega}}{d\sigma_{sub/d\Omega}}$$

Clearly this ratio, an expression of the sensitivity, should be as large as possible. When the force between the incoming ions and the target is a Coulomb force and the distance of closest approach is small compared to atomic dimensions yet large compared to those of the nucleus, then the Rutherford differential cross section can be expressed in the laboratory coordinates as

$$\frac{d\sigma}{d\Omega}(E) = \left[\frac{Z_1 Z_2 e^2}{4E}\right]^2 \frac{4}{\sin^4\psi} \frac{\left[\left[1 - \left(\frac{m_1}{m_2}\sin\psi\right)^2\right]^{\frac{1}{2}} + \cos\psi\right]^2}{\left[1 - \left(\frac{m_1}{m_2}\sin\psi\right)^2\right]^{\frac{1}{2}}}$$

where $e^2 = \frac{q^2}{4\pi\varepsilon_o}$

From this expression and the graph of $d\sigma/d\Omega$ vs m_1 in Fig. 6, a couple of relationships can be noted:

1) The cross section increases as the square of the incident charge, Z_1^2. Since the beam's charge generally increases as its mass does, this enhancement can be accomplished by increasing the incident mass. As an example, the yield from a $^{19}_{7}F$ beam will be about 12 times larger than the yield from a $^{4}_{2}He$ beam.
2) The cross section, and thus the sensitivity, increases as the incident mass, m_1, increases.

As a summary, it has been predicted that for backscattering angles near 180 degrees (and with the restriction that the beam ions be lighter than the target atoms), beam ions heavier than the traditionally used $^{1}_{1}H^{+}$ or $^{4}_{2}He^{+}$ will result in better kinematic separation, better mass resolution, better depth resolution as a consequence of greater energy loss, and increased sensitivity to the target atoms.

FIG. 6 Graph of the differential cross section vs incident mass where each curve represents a different target element. the beam has an incident energy of E_o = 17.5 MeV and backscatters at $\psi = 150^{o}$.

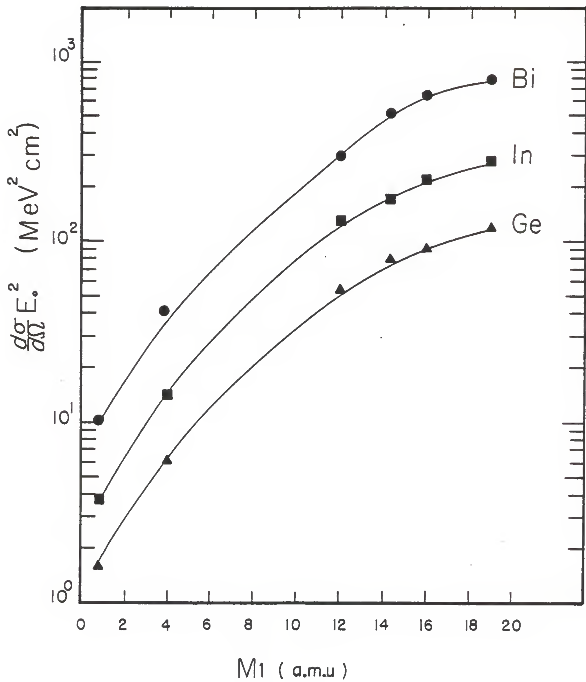
10^3
10^2
10^1
10^0
$\frac{d\sigma}{d\Omega}E_0^2$ (MeV^2 cm^2)
Bi
In
Ge
0
2
4
6
8
10
12
14
16
18
20
M1 (a.m.u)

Chapter 3

EXPERIMENT

A Lambda Physik model EMG100 XeCl excimer laser was used to anneal the samples. The laser pulse had an energy density of $0.8 J/cm^2$ or $1.0 J/cm^2$ and a duration of about 10 nsec. The sample was mechanically scanned so that each spot received 10 pulses.

Prior to the RBS measurements, the samples were cleaned with acetone and mounted on the target holders with Eccotherm TC-4. The Eccotherm fluoresced on the edge of the sample where the ion beam was incident so that it was possible to estimate the position of the beam before a spectrum was taken. After the measurement the beam spot on the sample was checked to make sure that the beam was in the desired region on the sample.

${}^4_2He^+$ RBS

For the Si samples, a ${}^4_2He^+$ beam at an incident energy of 1.5 MeV was used. The source of the beam was the 3MV electrostatic Van de Graaff accelerator at Kansas State University, see Fig. 7.

The backscattering chamber was designed in such a way that the maximum backscattering angle, ψ, was 150 degrees for a normal incidence beam. Three samples could be attached to the target ladder in the chamber at one time. The beam was collimated to a 2mm diameter spot size on the sample. Typical pressures in the chamber were between 10^{-6} and 10^{-7} Torr.

Fig. 7 Schematic of AK-N single stage 3MV Van de Graaff accelerator.[4]

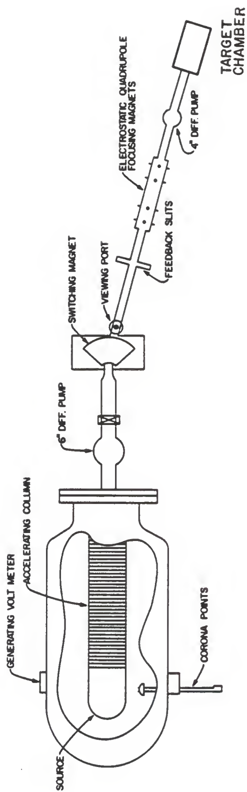
3MV VAN DE GRAAFF
GENERATING VOLT METER
ACCELERATING COLUMN
SOURCE
CORONA POINTS
6" DIFF. PUMP
SWITCHING MAGNET
VIEWING PORT
FEEDBACK SLITS
ELECTROSTATIC QUADRUPOLE
FOCUSING MAGNETS
4" DIFF. PUMP
TARGET
CHAMBER

Beam current on the target was approximately 5nA. Data were collected on a single sample until there were at least 100 counts in the impurity peak channel with the most counts. Aquisition time for one acceptable spectrum was about 30 minutes.

The detector used to measure the energy of the backscattered He particles was an Ortec Si surface barrier detector, 100 micrometers in depth. The detector received a bias voltage of 150V from an Ortec 210 Detector Control Unit. Pulses from the detector were amplified first by an Ortec 142 Preamplifier and then by an Ortec 450 Amplifier. Finally a pulse-height spectrum of 512 channels from a ND100 Multichannel Analyzer was recorded on magnetic tape.

A spectrum from an alpha source, ^{241}Am, was taken to check the resolution of the system. The full width at half maximum (FWHM) of the ^{241}Am peak was 2 channels which corresponds to a resolution of approximately 30 keV.

$^{19}F^{4+}$ HIRBS

A flourine ion beam of energy 17.5 MeV was used for the Heavy Ion Rutherford Backscattering (HIRBS) on Ge. The source of the beam was the electrostatic 6 MV model EN tandem Van de Graaff accelerator in the James R. Macdonald Laboratory at Kansas State University, See Fig. 8.

The experimental station featuring a 61.0 cm diameter chamber was used for the HIRBS. The chamber contained a target ladder capable of

Fig. 8 Schematic of Tandem Van de Graaff Accelerator.[5]

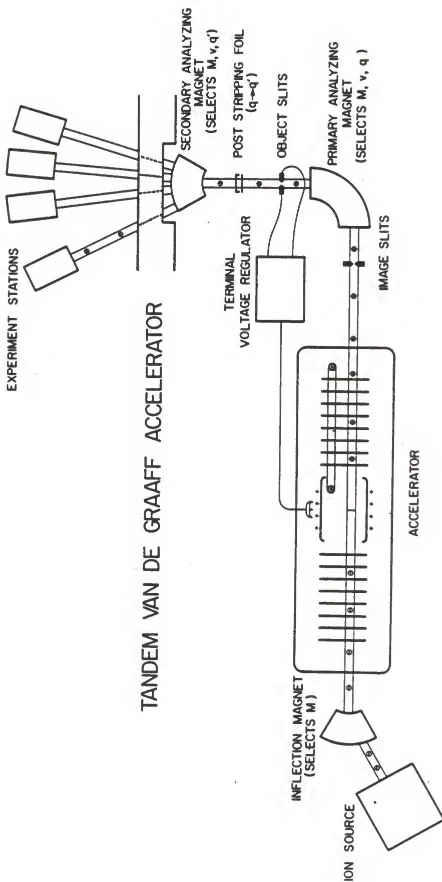
TANDEM VAN DE GRAAFF ACCELERATOR
EXPERIMENT STATIONS
SECONDARY ANALYZING MAGNET (SELECTS M, v, q')
POST STRIPPING FOIL (q→q')
OBJECT SLITS
PRIMARY ANALYZING MAGNET (SELECTS M, v, q)
TERMINAL VOLTAGE REGULATOR
IMAGE SLITS
ACCELERATOR
INFLECTION MAGNET (SELECTS M)
ION SOURCE

holding five samples. Typical pressures ranged from 10^{-6} to 10^{-7} Torr. The beam, which was collimated to a 2mm diameter spot on the sample, was normally incident on the sample and was detected at 150 degrees with respect to the incident beam. Although the detector angle was adjustable and an angle closer to 180 degrees would result in better resolution, the angle 150 degrees was chosen so that a comparison between a heavy ion beam (^{19}F) and a light ion beam (^{4}He) could be performed at the same angle. The detector angle on the chamber on the He beam accelerator was limited to 150 degrees.

The current on the target was typically 50 nA which made aquisition time for an acceptable spectrum (ie. more than 100 in the impurity channel with the most counts) usually less than 15 min.

The detector used to measure the energy of the backscattered F^{4+} ions was an Ortec Si surface barrier detector, 100 micrometers in thickness. A bias voltage of 80 Volts was supplied to the detector by an Ortec 210 Detector Control Unit. The pulses from the detector were amplified first by a Tennelec TC133 Preamplifier and then by an Canberra 2010 Spectroscopy Amplifier. A pulse-height spectrum of 1024 channels from a Canberra 8100 Multichannel Analyzer was then recorded on magnetic tape.

An upper limit to the resolution of the system was obtained by measuring the FWHM of a very thin carbon foil (5micrograms/cm^2) to obtain 20 channels (150 keV) resolution.

Chapter 4

DATA ANALYSIS

A spectrum obtained from the multichannel analyzer used in the Si studies is shown in Fig. 9. The quality of these spectra (due to low beam current) was such that data manipulation, such as pile-up stripping, was not necessary. However this was not the case for the Ge spectra.

An example of a spectrum obtained from the multichannel analyzer in HIRBS is shown in Fig. 10. Pile-up occurs when two or more simultaneous pulses combine to form one pulse whose energy is the sum of the combined pulses' energies. Because the counts were detected at a fast rate, pile-up can be a problem in this experiment. Also, the fact that the samples are thick (approximately 2mm) means that there are many combinations of the lower energies (channels) that can combine to form one high energy pulse in the region of interest (ie. near the impurity peak). In order to strip the pile-up spectrum from the raw spectrum, a program was written which numerically convolutes the substrate peak and then scales that curve to fit the pile-up in the spectrum. However, this is an extremely slow process. The alternative is to analytically convolute the substrate peak. The probability that a pile-up count is produced in channel C_1 is (See Fig. 11)

$$P(C_1) = A \int_{C_{LO}}^{C_{HI}} P(C_o)\, P(C_1 - C_o)\, dC_o$$

Fig. 9 RBS spectrum of as-implanted Si:As at a dose of 1 X 10^{17}as cm^{-2}using a 1.5 MeV ^{4}He beam, $\psi = 150^{\circ}$.

Fig. 10 HIRBS spectrum of as-implanted Ge:Bi at a dose of 1 X 10^{16} Bi cm^{-2} using a 17.5 MeV ^{19}F beam, $\psi = 150^{\circ}$.

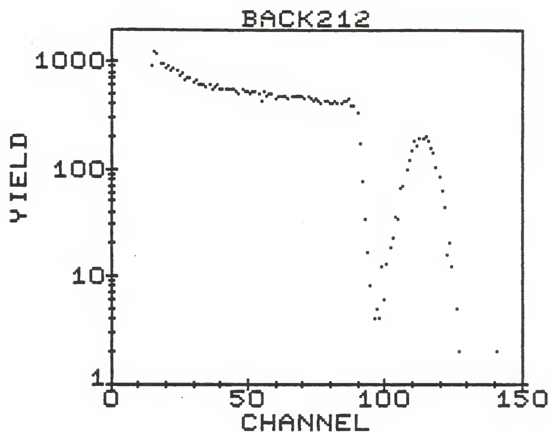
BACK212
YIELD
1000
100
10
1
CHANNEL
0
50
100
150

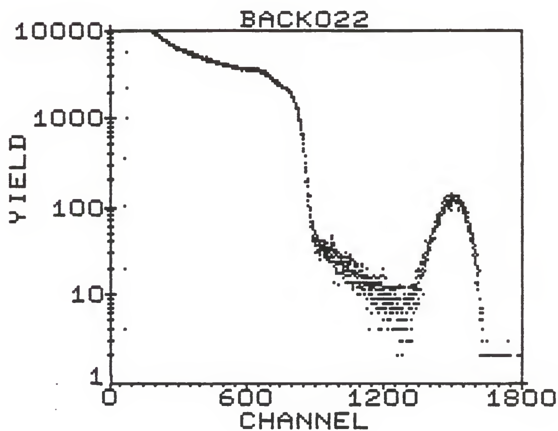
BACK022
YIELD
10000
1000
100
10
1
CHANNEL
0
600
1200
1800

Fig. 11 Schematic of a spectrum exhibiting pile-up in the region of the impurity peak.

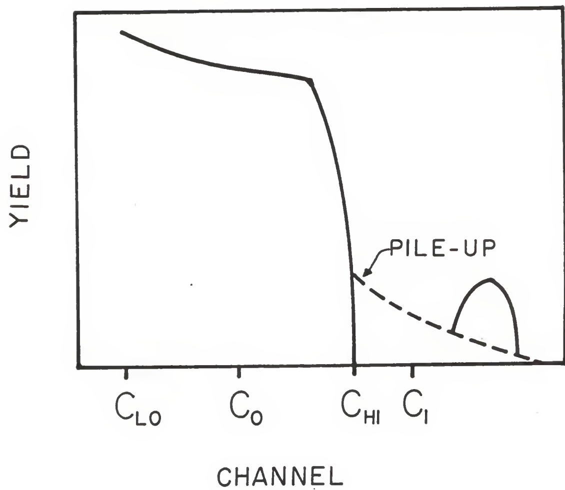
YIELD
PILE-UP
C_{LO}
C_O
C_{HI}
C_I
CHANNEL

where $P(C_o)$ is the probability that a count appears in C_o

A is a normalization factor

since $Y \propto \frac{d\sigma}{d\Omega} \propto \frac{1}{C^2}$

then $P(C_o) \propto \frac{1}{C_o^{\,2}}$

thus $N(C_1) = B \int_{C_{LO}}^{C_{HI}} \frac{dC_o}{C_o^{\,2}(C_1-C_o)^2}$

$$= \frac{B}{C_1^{\,2}} \left[\frac{1}{(C_1-C_o)} - \frac{1}{C_o} + \frac{2}{C_1} \ln\left(\frac{C_o}{C_1-C_o}\right)\right]$$

where $N(C_1)$ is the number of pile-up counts in C_1

B is a constant chosen to best fit the pile-up spectrum.

The final spectra were not only stripped of the pile-up (see Fig. 12), but were also averaged in such a way that one data point represents the average of the ten consecutive points surrounding it. Since the resolution was greater than ten channels, this last step just reduced the number of data points. An example of the final product is shown in Fig. 13.

Fig. 12 HIRBS spectrum, of the same sample shown in Fig. 8, which has been stripped of pile-up.

Fig. 13 HIRBS spectrum, of the same sample shown in Fig. 8, which has been stripped of pile-up and the number of points has been condensed.

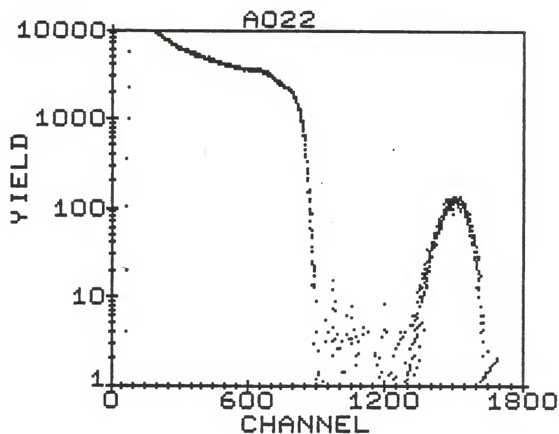

A022
10000
1000
100
10
1
YIELD
0
600
1200
1800
CHANNEL

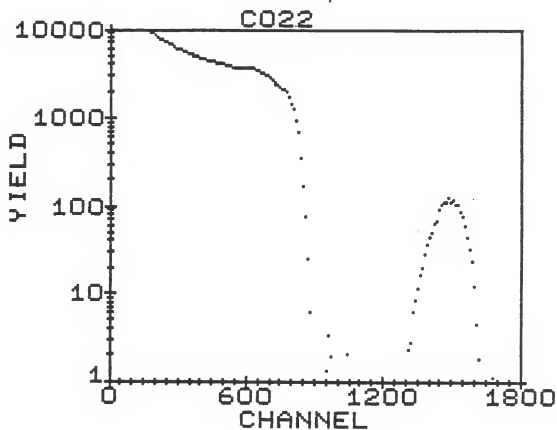

C022
10000
1000
100
10
1
YIELD
0
600
1200
1800
CHANNEL

X AXIS SCALES

The conversion of the x axis from channel number to energy can be found using the channel where the yield is half of the maximum yield in the peak corresponding to a particular element that lies on the surface of the crystal. This channel is chosen as its surface channel. An example of a spectrum chosen for the calibration in the Ge studies is shown in Fig. 14 where because of annealing it is evident that the Bi has segregated to the surface.

Thus at the surface, the energy of the detected particles is

$$E(C_{Ge}) = E_o \, K_{Ge}$$

$$E(C_{Bi}) = E_o \, K_{Bi}$$

where E_o=17.5 MeV

$$K = \left[\frac{(m_2^2 - m_1^2 \sin^2\psi)^{\frac{1}{2}} + m_1 \cos\psi}{m_1 + m_2} \right]^2$$

where m_1 = 19 for F beam mass

m_2 = 209 or 73 for Bi or Ge target mass

$\psi = 150^o$

In this case the energy conversion is 7.6 keV/channel.

Fig. 14 HIRBS spectrum of pulsed laser annealed Ge:Bi at a dose of 1 X 10^{16} Bi cm^{-2} using 17.5 MeV ^{19}F beam $\psi = 150^{o}$. The impurity has segrated to the surface.

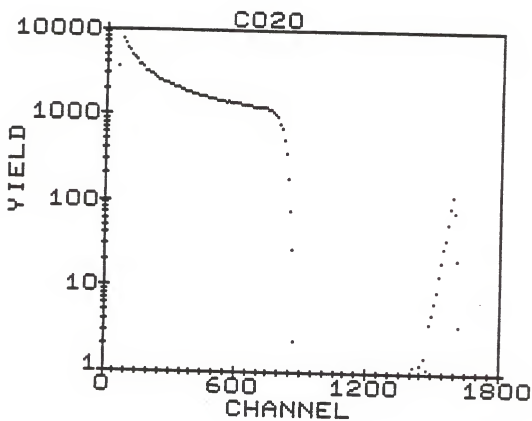
C020
10000
1000
100
10
1
YIELD
0
600
1200
1800
CHANNEL

This can be used to find a conversion from channel to depth for each peak. As before

$$\frac{\text{depth}}{\text{channel}} = \frac{7.6\ (^{\text{keV}}/\text{channel})}{\left[K - \frac{1}{\cos\psi}\right] \left.\frac{dE}{dx}\right|_{E_0} (^{\text{keV}}/_{\mu m})}$$

where $\left.\frac{dE}{dx}\right|_{E_0} = 2885\ \text{keV}/\mu m$[6]

A summary of the depth conversions for each element is shown in Table 1.

Y AXIS SCALES

The y axis of each element in counts/channel can be converted to concentration in ions/cm^3. The equation for the yield in channel i is

$$Y_i = \frac{d\sigma}{d\Omega}(E_i)\ Y_0\ d\Omega\ Nt$$

The ratio of the impurity peak to the substrate peak becomes

$$\frac{Y_{imp}}{Y_{sub}} = \frac{d\sigma_{imp}/d\Omega\ N_{imp}\ t_{imp}}{d\sigma_{sub}/d\Omega\ N_{sub}\ t_{sub}}$$

Ge samples using a 17.5 MeV ^{19}F beam, $\psi = 150^{o}$

target	E_0K (MeV)	depth conversion (Å/channel)
^{73}Ge	6.47	17.23
^{115}In	9.39	15.57
^{122}Sb	9.74	15.39
^{209}Bi	12.45	14.11

Si samples using a 1.5 MeV ^{4}He beam, $\psi = 150^{o}$.

target	E_0K (MeV)	depth conversion (Å/channel)
^{28}Si	0.877	222.0
^{75}As	1.229	196.0
^{115}In	1.317	190.0

Table 1

By choosing a constant yield for the substrate, Y_{sub}, over the interval to be considered, the relationship between the impurity yield, Y_{imp}, and impurity concentration, N_{imp}, can be made linear

$$Y_{imp} = \frac{Y_{sub} \, {}^{d\sigma_{imp}}/_{d\Omega} \, t_{imp}}{N_{sub} \, {}^{d\sigma_{sub}}/_{d\Omega} \, t_{sub}} \quad N_{imp}$$

This last equation assumes that the density of the substrate, N_{sub}, and thus the width of a channel in either peak, t, is constant over the interval of interest. However it can be seen from the substrate edge in Fig. 15 that this was not the case for the as-implanted Ge samples.

Discussion of this apparent decrease in the substrate density of Ge has only recently appeared in the literature.[7,8,9] At large doses, the Ge substrate forms deep craters (on the order of .1microns) which are normal to the surface, independent of the angle of implantation. This porous structure, although not formed during liquid nitrogen implants, is readily formed at room temperature implants (as is the case in these experiments). This crater formation has not been observed in implanted Si substrates at these doses.

The spectra obtained from RBS and HIRBS, arranged according to implant mass and dose, are shown in Fig. 16 through Fig. 20.

Fig. 15 HIRBS spectrum of as-implanted Ge:Sb at a dose of 2×10^{16} Sb cm^{-2} using 17.5 MeV ^{19}F beam, $\psi = 150^{\circ}$. The dip at the edge of the substrate peak represents a density deficiency at the surface of the crystal.

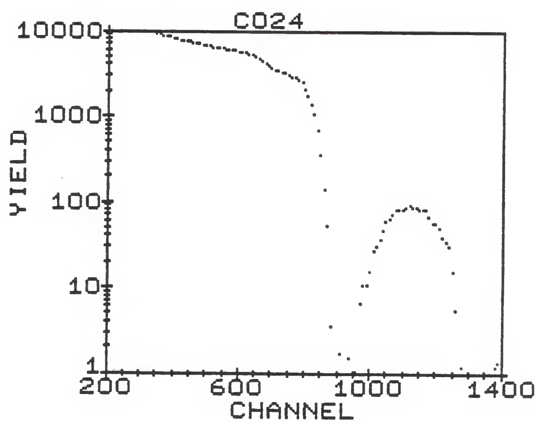
C024
10000
1000
100
10
1
YIELD
200
600
1000
1400
CHANNEL

Fig. 16 HIRBS spectra using a 17.5 MeV ^{19}F beam, $\psi = 150^{\circ}$ on:

a) as-implanted Ge:In, dose 1 X 10^{16} In cm^{-2}.

b) annealed Ge:In, dose 1 X 10^{16} In cm^{-2}.

c) as-implanted Ge:In, dose 2 X 10^{16} In cm^{-2}.

d) annealed Ge:In, dose 2 x 10^{16} In cm^{-2}.

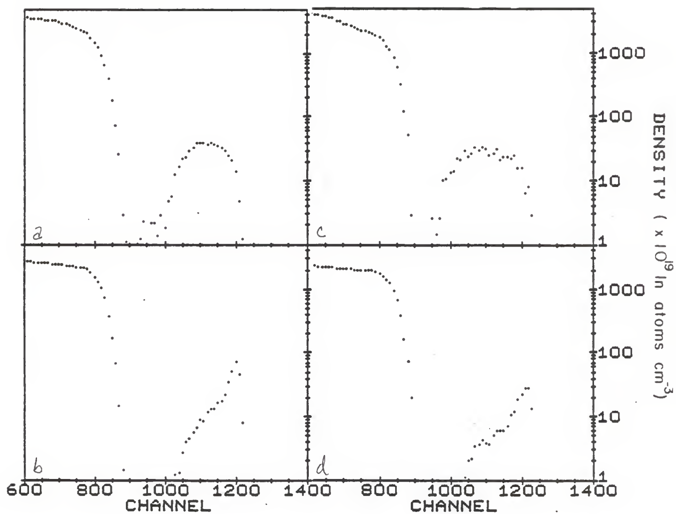
a
b
c
d
1000
100
10
1
600
800
1000
1200
1400
CHANNEL
DENSITY (x 10^19 In atoms cm^-3)

Fig. 17 HIRBS spectra using a 17.5 MeV
^{19}F beam, $\psi = 150^{\circ}$ on:

a) as-implanted Ge:Sb, Dose 1×10^{16} Sb cm^{-2}.

b) low annealed (0.8 J/cm^2) Ge:Sb, Dose 1×10^{16} Sb cm^{-2}.

c) high annealed (1.0 J/cm^2) Ge:Sb, Dose 1×10^{16} Sb cm^{-2}.

d) as-implanted Ge:Sb, Dose 2×10^{16} Sb cm^{-2}.

e) low annealed (0.8 J/cm^2) Ge:Sb, Dose 2×10^{16} Sb cm^{-2}.

f) high annealed (1.0 J/cm^2) Ge:Sb, Dose 2×10^{16} Sb cm^{-2}.

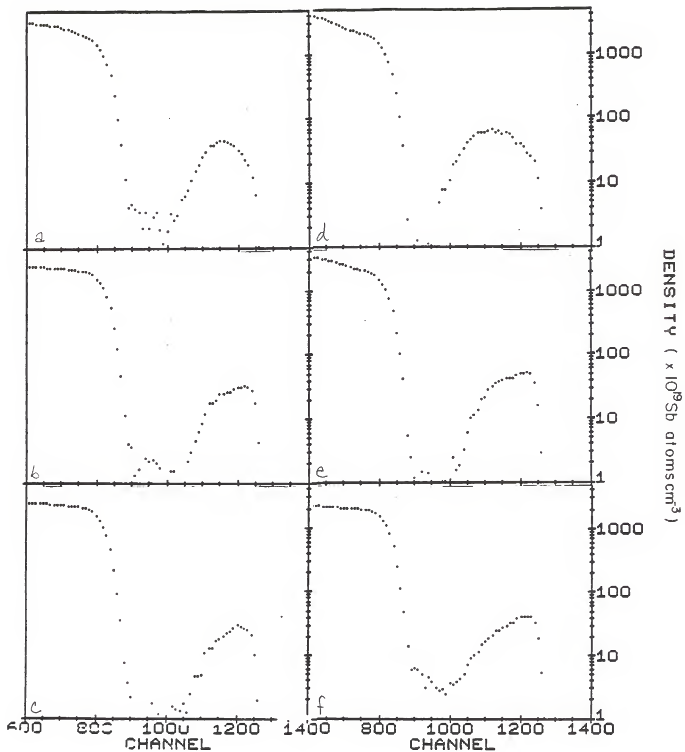

a
b
c
d
e
f
1000
100
10
1
600
800
1000
1200
1400
CHANNEL
DENSITY (x 10^{19}Sb atoms cm^{-3})

Fig. 18 HIRBS spectra using a 17.5 MeV ^{19}F beam, $\psi = 150^{o}$ on:

a) as-implanted Ge:Bi, dose 1 X 10^{16} Bi cm^{-2}.

b) annealed Ge:Bi, dose 1 x 10^{16} Bi cm^{-2}.

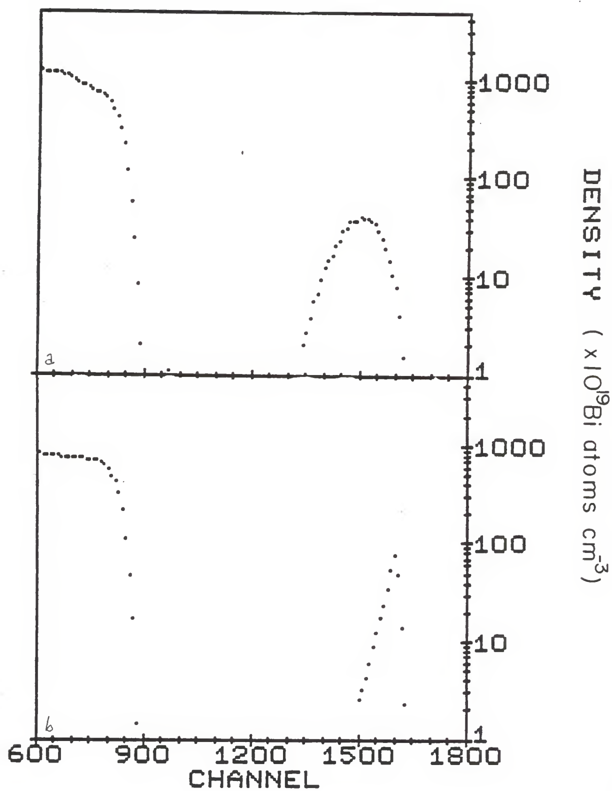

a
b
1000
100
10
1
DENSITY (x10^{19}Bi atoms cm^{-3})
600
900
1200
1500
1800
CHANNEL

Fig. 19 RBS spectra using a 1.5 MeV ^4He beam, $\psi = 150^o$ on:

a) low annealed (0.8 J/cm^2) Si:As, dose 2×10^{16} As cm^{-2}.

b) high annealed (1.0 J/cm^2) Si:As, dose 2×10^{16} As cm^{-2}.

c) as-implanted Si:As, dose 1×10^{17} As cm^{-2}.

d) annealed Si:As, dose 1×10^{17} As cm^{-2}.

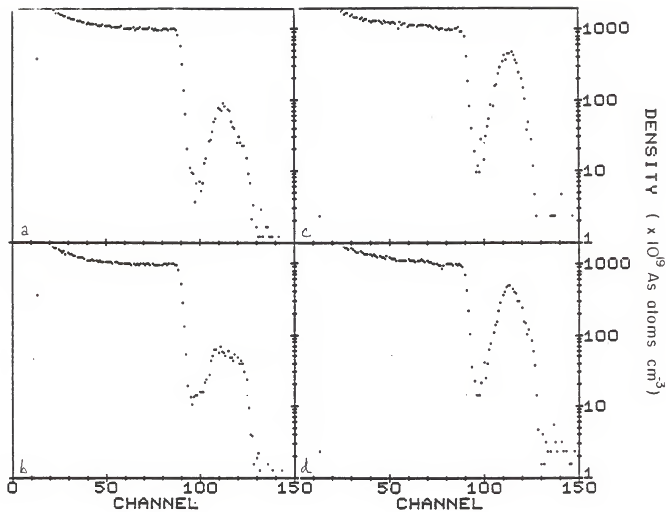
a
b
c
d
0
50
100
150
CHANNEL
1000
100
10
1
DENSITY (x 10^19 As atoms cm^-3)

Fig. 20 HIRBS spectra using a 1.5 MeV ^{4}He beam, $\psi = 150^\circ$ on:

a) as-implanted Si:In, dose 1 X 10^{16} In cm^{-2}.

b) annealed Si:In, dose 1 x 10^{16} In cm^{-2}.

c) as-implanted Si:In, dose 2 x 10^{16} In cm^{-2}.

d) annealed Si:In, dose 2 X 10^{16} In cm^{-2}.

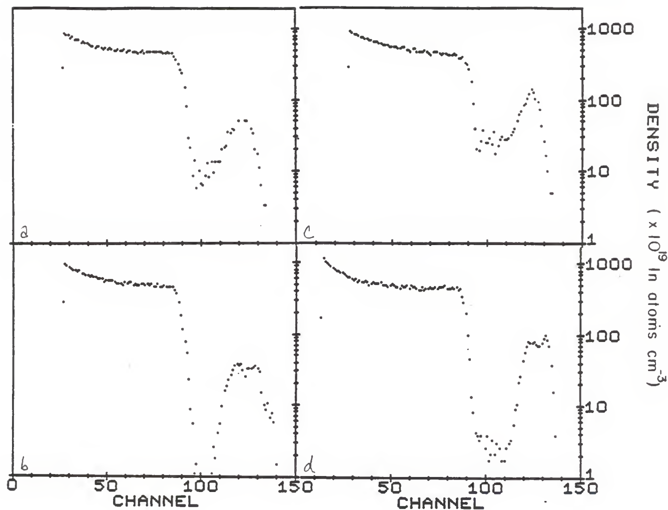

a
c
b
d
1000
100
10
1
0
50
100
150
CHANNEL
DENSITY (x 10^19 In atoms cm^-3)

Chapter 5

RESULTS

With the conversion of the x axis at the impurity peak from channel to depth, a quantitative comparison between measured and predicted projected standard deviations and ranges[10] can be made. From the values in Table 2, the measured range of the implanted ions in Si is somewhat larger than predicted, and the width of the peak is significantly broader than predicted. Both the projected range and projected standard deviation appear to increase with implant mass, but not with dose. One possible explanation for this effect is that of inadvertant channeling. Recent experiments have questioned the effectivness of the 7 degree tilt popularly used to obtain a "random equivalent" implant.[11] Another possibility is that diffusion occurs during implantation due to the heat produced during implantation at room temperature.[12]

The effect of pulsed laser annealing on the impurity distribution of the Si samples is to broaden the peak. Table 3 is a list of FWHM values for the spectra and the relative difference between the as-implanted and corresponding annealed FWHM values.

For the Ge samples, from Table 4 again it is evident that the measured projected standard deviations are much larger than the predicted standard deviations. The relative difference is as much as five times larger, as in the case of Bi implanted Ge. This could be due to inadvertent channeling as was suggested for the Si samples. However, unlike the Si samples, the relative differences seem to have a dependence

as-implanted	range (Å)		standard deviation (Å)		relative difference	
	observed r_o	predicted r_p	observed σ_o	predicted σ_p	$\frac{r_o - r_p}{r_p}$	$\frac{\sigma_o - \sigma_p}{\sigma_p}$
Si:As, $1 \times 10^{17} cm^{-2}$	1960	1923	920	352	0.2	1.60
Si:In, 1×10^{16} cm^{-2}	2090	1360	1160	205	0.54	4.64
Si:In, 2×10^{16} cm^{-2}	1880	1360	800	205	0.38	2.90
Si:Sb, 1×10^{16} cm^{-2}	2290	1322	1150	194	0.73	4.93

Table 2

	FWHM (Å)	relative difference $\frac{FWHM_{ann}-FWHM_{a-i}}{FWHM_{a-i}}$
Si:As 2 x 10^{16} cm^{-2} ,low annealed	2160	0.63
Si:As 2 x 10^{16} cm^{-2} ,high annealed	3530	
Si:As 1 x 10^{17} cm^{-2} ,as-implanted	2160	0.09
Si:As 1 x 10^{17} cm^{-2} ,annealed	2350	
Si:In 1 x 10^{16} cm^{-2} ,as-implanted	2720	0.23
Si:In 1 x 10^{16} cm^{-2} ,annealed	3340	
Si:In 2 x 10^{16} cm^{-2},as-implanted	1880	0.41
Si:In 2 x 10^{16} cm^{-2},annealed	2660	

Table 3

as-implanted	range (Å)		standard deviation (Å)		relative difference	
	observed r_o	predicted r_p	observed σ_o	predicted σ_p	$\frac{r_o - r_p}{r_p}$	$\frac{\sigma_o - \sigma_p}{\sigma_p}$
Ge:In, 1×10^{16} cm^{-2}	1560	867	930	251	0.80	2.69
Ge:In, 2×10^{16} cm^{-2}	2030	867	1130	251	1.34	3.48
Ge:Sb, 1×10^{16} cm^{-2}	1540	840	780	238	0.83	2.29
Ge:Sb, 2×10^{16} cm^{-2}	2160	840	1110	238	1.57	3.67
Ge:Bi, 1×10^{16} cm^{-2}	1550	609	780	131	1.55	4.95

Table 4

on the dose of the implant. By comparing different doses of the same implant, the data suggest that the relative difference increases with dose.

Again from the table comparing measured and predicted projected ranges of the implant in the Ge substrate, it is clear that the measured projected ranges are consistently larger than the predicted values Moreover, the relative differences increase with the mass as well as the dose of the implant.

These results might be more surprising were it not for a recently discovered morphological change that the Ge surface undergoes upon bombardment at room temperature. According to B.R. Appleton et al.,[13] the surface of Ge becomes amorphous for moderate doses up to 10^{15} cm^{-2} at room temperature. However, for doses beyond 10^{15} cm^{-2}(as is the case in these experiments) the surface develops a morphological instability, initiated in the amorphous phase, which results in the formation of surface craters several hundred nanometers deep. The anomalous structure can anneal away although recrystallization is somewhat retarded by the porous structure.[14]

This porous structure is indicated in our experiments as an apparent density deficiency in the Ge surface peak of the as-implanted spectra relative to the annealed spectra. This is most evident in the following spectra, Fig. 21, where the yield in each as-implanted Ge peak channel has been divided by the yield in the same channel of the corresponding annealed Ge sample spectrum.

By comparing different doses of the same implant, the data also indicate that the depth into the substrate of the density deficiency increases with the dose. That is, the depth of the craters increases

Fig. 21 HIRBS spectra using a 17.5 MeV ^{17}F beam, $\psi = 150^\circ$. Relative density values were obtained by dividing the yield of each as-implanted spectrum channel by the corresponding yield in the annealed spectrum at the substrate peak edge.

a) Ge:In, dose 1×10^{16} In cm^{-2}.

b) Ge:In, dose 2×10^{16} In cm^{-2}.

c) Ge:Sb, dose 1×10^{16} Sb cm^{-2}.

d) Ge:Sb, dose 2×10^{16} Sb cm^{-2}.

e) Ge:Bi, dose 1×10^{16} Bi cm^{-2}.

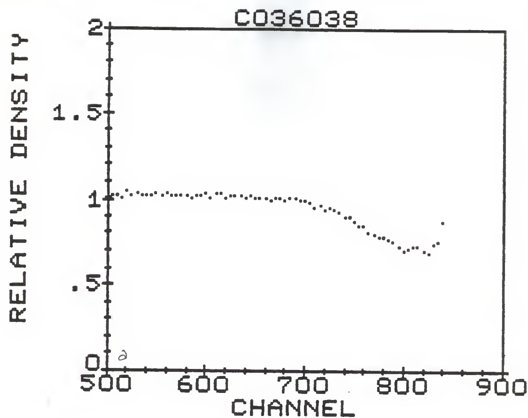
C036038
RELATIVE DENSITY
2
1.5
1
.5
0
a
500
600
700
800
900
CHANNEL

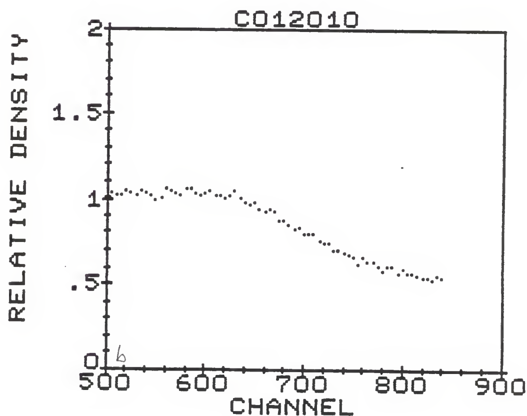
C012010
RELATIVE DENSITY
2
1.5
1
.5
0
b
500
600
700
800
900
CHANNEL

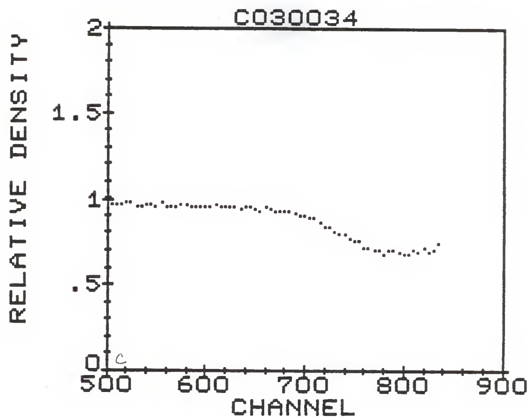
C030034
RELATIVE DENSITY
2
1.5
1
.5
0
c
500
600
700
800
900
CHANNEL

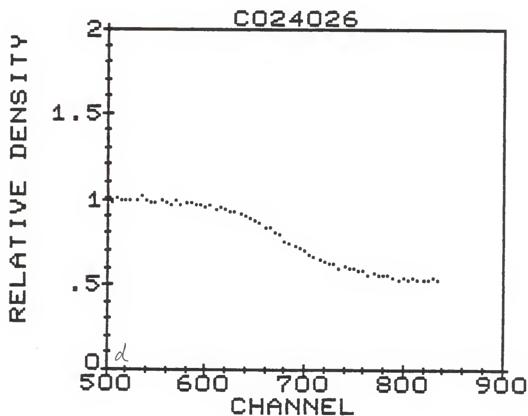
C024026
RELATIVE DENSITY
2
1.5
1
.5
0
d
500
600
700
800
900
CHANNEL

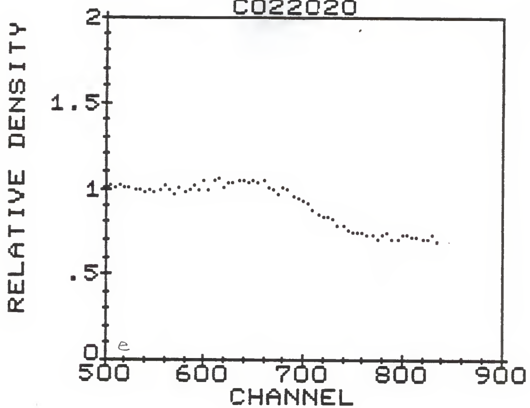
C022020
RELATIVE DENSITY
2
1.5
1
.5
0
500
600
700
800
900
CHANNEL
e

with dose. This is also noted by Appleton. The fact that the density deficiency increases with increased dose suggests that the areal density of the craters increases with larger doses. Appleton also notes that the crater formation increases with increased mass of the implant. This is not apparent from the spectra of relative density, but might be indicated in the tables of standard deviation and range relative differences.

Finally, the formation and existence of craters at the surface during implantion would explain the large relative difference in standard deviation and in projected range in all as-implanted Ge samples. The ions to be implanted could travel farther into the sample than predicted if they entered a crater. On the other hand, although the RBS beam has the possibility of partially entering a crater, it is measured at an angle not normal to the surface and thus will detect the implanted ions at a depth relative to an average surface depth, not to the individual crater's depth. This results in a spectrum indicating large range and standard deviation.

Because of the anomalous broadening of the as-implanted peak in the Ge samples due to crater formation, it is difficult to make a general comparison between as-implanted and annealed spectra FWHM values to determine the effectiveness of pulsed laser annealing, Table 5. There is an added complication in the Ge:In and Ge:Bi samples where much of the implant has segregated to the surface.

Fig. 22 is a schematic equilibrium phase diagram appropriate for each of the implant plus substrate systems considered here. The solid dopant concentration passes through a maximum known as the retrograde maximum dopant concentration, C_S. Baker and Cahn[15] have shown that for retrograde alloys such as these, the retrograde maximum concentration cannot be ex-

	FWHM (A)	relative difference $\frac{FWHM_{ann}-FWHM_{a-i}}{FWHM_{a-i}}$
Ge:In 1×10^{16} cm^{-2} as-implanted Ge:In 1×10^{16} cm^{-2} annealed	2180 470	-.78
Ge:In 2×10^{16} cm^{-2} as-implanted Ge:In 2×10^{16} cm^{-2} annealed	2650 780	-.71
Ge:Sb 1×10^{16} cm^{-2} as-implanted Ge:Sb 1×10^{16} cm^{-2} low annealed Ge:Sb 1×10^{16} cm^{-2} high annealed	1850 1850 1540	-.17
Ge:Sb 2×10^{16} cm^{-2} as-implanted Ge:Sb 2×10^{16} cm^{-2} low annealed Ge:Sb 2×10^{16} cm^{-2} high annealed	2620 2000 2000	-.24
Ge:Bi 1×10^{16} cm^{-2} as-implanted Ge:Bi 1×10^{16} cm^{-2} annealed	1840 420	.77

Table 5

Fig. 22 Schematic of an equilibrium phase diagram for the implant plus substrate systems.[16]

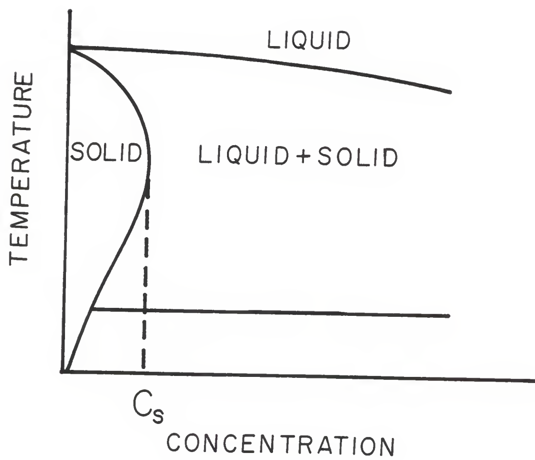

LIQUID
TEMPERATURE
SOLID
LIQUID + SOLID
C_S
CONCENTRATION

ceeded in an equilibrium solidification process. The fact that solubility limits greater than the retrograde solubility limit have been achieved using pulsed laser annealing indicates a non-equilibrium process. This process is a result of high interface velocities (several meters/second) in which the dopants do not exchange a sufficient number of times between the solid and liquid interface to establish their equilibrium concentration.

The observed peak concentration of each annealed sample in this experiment and the retrograde solubility limits are shown in Table 6. Since these concentration values were calculated from the RBS spectrum and not from ion channeling, they are not necessarily substitutional concentrations. However, in general liquid phase epitaxial regrowth from the undamaged crystal (as is the case in these experiments) incorporates the dopants into lattice sites and forces those not incorporated to the surface. This clearly happens in both annealed Ge:In samples. In this instance the peak concentration was determined by excluding the large surface peak. In the Ge:Bi sample, it appears that essentially all of the dopant segregated to the surface so that it was not possible to estimate a peak concentration while excluding the surface peak.

It should be noted that the peak concentrations increase with increased implant dose and with decreased energy density.

Narayan predicts that higher interface velocities would result in higher substitutional concentrations.[17] It was previously noted that the porous structure (present in the as-implanted Ge samples) inhibits the regrowth interface velocity. Thus it might be expected that samples without the porous structure (ie. those implanted at liquid nitrogen temperature)[18] would have faster interface velocities and thus larger subtitutional maximum concentrations.

Table 7 is a comparison of the predicted impurity dose and the dose obtained by integrating the impurity peak on the density vs. depth spectra. It is clear that there is a loss of impurity atoms during implantation as well as annealing. Moreover, the loss increases with annealing energy density.

	dose $\left(\frac{\text{ions}}{\text{cm}^2}\right)$	max concentration $\left(\frac{\text{atoms}}{\text{cm}^3}\right)$	$C_s\left(\frac{\text{atoms}}{\text{cm}^3}\right)$
Ge:In	1×10^{16}	2.5×10^{20}	3×10^{20}
Ge:In	2×10^{16}	6.0×10^{19}	
Ge:Sb	1×10^{16} low ann	3.5×10^{20}	
Ge:Sb	1×10^{16} hi ann	3.0×10^{20}	1.2×10^{19}
Ge:Sb	2×10^{16} low ann	5.0×10^{20}	
Ge:Sb	2×10^{16} hi ann	4.0×10^{20}	
Ge:Bi	1×10^{16}	---	
Si:As	2×10^{16} lo ann	9×10^{20}	
Si:As	2×10^{16} hi ann	7×10^{20}	1.8×10^{21}
Si:As	1×10^{17}	5×10^{21}	
Si:In	1×10^{16}	3×10^{20}	
Si:In	2×10^{16}	8×10^{20}	8×10^{17}

Table 6

	predicted dose $\left(\frac{atoms}{cm^3}\right)$	measured dose $\left(\frac{atoms}{cm^3}\right)$
Ge:In as-implanted	1×10^{16}	9×10^{15}
Ge:In annealed	1×10^{16}	6×10^{15}
Ge:In as-implanted	2×10^{16}	9×10^{15}
Ge:In annealed	2×10^{16}	3×10^{15}
Ge:Sb as-implanted	1×10^{16}	9×10^{15}
Ge:Sb low annealed	1×10^{16}	6×10^{15}
Ge:Sb high annealed	1×10^{16}	5×10^{15}
Ge:Sb as-implanted	2×10^{16}	2×10^{16}
Ge:Sb low annealed	2×10^{16}	1×10^{16}
Ge:Sb high annealed	2×10^{16}	9×10^{15}
Ge:Bi as-implanted	1×10^{16}	8×10^{15}
Ge:Bi annealed	1×10^{16}	4×10^{15}

Table 7

Chapter 6

CONCLUSION

It has been shown that heavy ion RBS enhances traditional proton or alpha RBS properties such as depth resolution, mass resolution, and beam sensitivity to the dopant in a semiconductor substrate. The ion beam mass must remain less than the target mass for backscattering to occur. Thus the extent to which these properties can be improved is limited. Also the decrease in energy resolution of the surface barrier detector due to heavy ion bombardment will add another limit to the system.[19] On the other hand, the depth resolution of this experiment could be improved further using a beam at grazing incidence and keeping the backscattering angle large.

Through the use of RBS and HIRBS, the effect of pulsed laser annealing on the width and concentration of various impurity distributions in Si and Ge were determined.

The existence of a porous structure on the surface of Ge formed during implantation appears in the HIRBS spectra as a density depletion on the edge of the substrate peak. According to the relative density spectra, the extent of this density depletion depends on both implant mass and dose.

There are two studies which should follow this experiment. First, a channeling experiment should be performed to determine the substitional concentration of the dopant. It is not possible to differentiate between substitutional and intersitial impurities using RBS analysis. Generally an impurity atom will not be electrically active if it is interstitial.

Second an experiment to determine the concentration of charge carriers should be performed. Light impurities, such as C and O are absorbed onto the surface of the porous structure of as-implanted Ge when exposed to air.[20] These impurities could inhibit carrier activation after annealing. Perhaps ion implantation should be carried out at liquid nitrogen temperature to suppress the porous structure formation. This could be followed by in situ annealing to prevent adsorption of these impurities.

REFERENCES

1. C. W. White, S. R. Wilson, B. R. Appleton, F. W. Young, Jr., J. Appl. Phys. 51, 738 (1980)
2. W. K. Chu, J. W. Mayer, M. A. Nicolet, Backscattering Spectrometry (Academic Press 1978) p. 24
3. L. C. Northcliffe, R. F. Schilling, Nuclear Data Tables, edited by K. Way (Academic Press, 1979) Vol. 7
4. J. Hall, Internal Resonance Raman Scattering of Characteristic Target K X-Rays in Thick Silicon Targets (1977)
5. J. Hall, Systematics of Single and Double K-Shell Vacancy Production in Titanium Bombarded by Heavy Ions (1981)
6. L. C. Northcliffe, R. F. Schilling, Nuclear Data Tables edited by K. Way (Academic Press 1970) Vol. 7
7. B. R. Appleton, Mat. Res. Soc Symp. Proc. (Elsevier Science Publishing Co., Inc. 1984) Vol. 27, p. 195
8. J. S. Williams, D. J. Chivers, R. G. Elliman, S. T. Johnson, E. M. Lawson, I. V. Mitchell, K. G. Orrman-Rossiter, A. P. Pogany, K. T. Short, Mat. Res. Soc. Symp. Proc. (Elsevier Science Publishing Co., Inc. 1984) Vol. 27 p. 205
9. B. R. Appleton, O. W. Holland, j. Narayan, D. E. Schow III, J. S. Williams, K. T. Short, E. Lawson, Appl Phys. Lett. 41, 711 (1982)
10. W. S. Johnson, J. F. Gibbons, LSS Projected Range Statistics in Semiconductors (Stanford University Bookstore, 1969)
11. J. F. Ziegler, R. F. Lever, Appl. Phys. Lett. 46, 358 (1985)
12. J. W. Mayer, L. Eriksson, J. S. Davies, Ion Implantation in Semiconductors (Academic Press 1970) p. 6

13. B. R. Appleton, Mat. Res. soc. Symp. Proc. (Elsevier Science Publishing Co., Inc. 1984) Vol. 27, p. 195

14. Ibid p.201

15. J. C. Baker, J. W. Cahn, Acta Metall. 17, 575 (1969)

16. F. Trumbore, Bell Syst. Tech. J. 39, 205 (1960)

17. B. R. Appleton, O. W. Holland, j. Narayan, D. E. Schow III, J. S. Williams, K. T. Short, E. Lawson, Appl. Phys. Lett. 41, 498 (1982)

18. O. W. Holland, B. R. Appleton, j. Narayan, J. Appl. Phys. 54, 2295 (1983)

19. R. T. Sullins, C. V. Barros Leite, E. A. Schweikert, J. Radioanal. Chem. 78, 173 (1983)

20. B. R. Appleton, Mat. Res. Soc. Symp. Proc. (Elsevier Science Publishing Co., Inc. 1984) Vol. 27 p. 197

RUTHERFORD BACKSCATTERING IN ION-IMPLANTED AND PULSED LASER ANNEALED Si AND Ge

by

SHANALYN KIGER

B.S., Kansas State University, 1984

AN ABSTRACT OF A MASTER'S THESIS

submitted in partial fulfillment of the

requirements for the degree

MASTER OF SCIENCE

Department of Physics

KANSAS STATE UNIVERSITY

Manhattan, Kansas

1985

ABSTRACT

The effects of pulsed laser annealing on the impurity distribution of ion implanted Si and Ge have been studied. Rutherford backscattering (RBS) with a 1.5 MeV $^{4}He^{+}$ beam was used to obtain depth profiles of the impurities in Si, while heavy ion Rutherford backscattering (HIRBS) with a 17.5 MeV $^{19}F^{4+}$ beam was used for the Ge samples.

The advantages of increasing the beam mass when observing an impurity in a heavy substrate are demonstrated both with the equations used in backscattering analysis and with the experimental results.

The HIRBS spectra exhibit an apparent density deficiency at the edge of the as-implanted Ge peak due to a porous structure formed in Ge during implantation at room temperature. The dependence of this density deficiency on implant mass and dose is discussed.

Pulsed laser annealing, because it is a non-equilibrium process, results in a maximum impurity concentration higher than that predicted by the retrograde solubility limit.